Fabrication and testing of a miniature H_2/O_2 and $MeOH/O_2$ fuel cell

Christopher Apblett [a,*], David Ingersoll [a], Plamen Atanassov [b],
Donald Maricle [c], S. Sarangapani [d]

[a] *Sandia National Laboratories, 1515 Eubank Blvd. SE, Albuquerque, NM 87185, United States*
[b] *University of New Mexico, 247 Farris Engineering Center, Albuquerque, NM 87131, United States*
[c] *Maricle Consulting, LLC, 226 Forest Lane, Glastonbury, CT 06033, United States*
[d] *ICET, Inc., 916 Pleasant St., Unit 12, Norwood, MA 02062, United States*

Abstract

The construction and performance of a small-scale fuel cell using traditional catalysts and membrane separators is discussed. Cell active area was 1 cm × 1 cm, with a total unit cell volume of 0.3 cm^3 each. Under well-hydrated conditions running under hydrogen and oxygen, these cells demonstrated over 600 mW cm^{-2} at 80 °C. Design of flow fields and the requirements for water management showed that flow channels that were too small may have resulted in early channel blockage on the cathode, leading to lower power. Miniature cells suffered from higher than expected interfacial resistance which increased with time and this may be due either to more difficult hydration control in the membrane at smaller dimensions, or less compression in the smaller scale size leading to higher flow field/diffusion layer interfacial resistances. Running single cells in methanol to alleviate hydration issues still showed much higher interfacial resistances, but cell performance was roughly 75 mW cm^{-2} at 80 °C in 1 M MeOH with 20 sccm of ambient pressure air, and 140 mW cm^{-2} in 1 M MeOH with 20 sccm ambient pressure O$_2$. Lower performance in MeOH may be attributed to swelling of the sealing gaskets in methanol, leading to increased interfacial resistances over time.
© 2006 Elsevier B.V. All rights reserved.

Keywords: Hydrogen; Methanol; Miniature; Fuel cell

1. Background and Introduction

Because power demands for portable electronics are increasing rapidly, and run times of portable batteries can become the limiting factor for many portable applications, much research has been focused in recent years on developing longer lasting, higher power density systems. Fuel cells have received attention for these applications due to the potential for fuel cells to be smaller and more efficient than the current battery chemistries that are in use. For example, a good Lithium polymer cell can have energy densities on the order of 800 Wh l^{-1}. Methanol fuels have an energy density of ∼5000 Wh l^{-1}, requiring the fuel cell to be only 16% efficient to be competitive with existing battery systems. However, developing robust, stable fuel cells that func-

tion under the wide variety of operating conditions has proven difficult. Additionally, fuel cells, being energy conversion systems rather than energy storage systems like batteries, must be capable of continuously drawing on a fuel storage tank to continuously provide power. This volume of fuel quickly becomes the single dominant volume in the fuel cell system. Still, miniaturization of the fuel cell allows for the maximum volume to be relegated to the fuel tank.

Several workers have developed miniature fuel cell systems in the past, and continue to develop these systems for small scale applications that will run on MeOH bases supply systems. Many workers have focused on using microelectromechanical systems (MEMS) technology by machining Si based devices to replace the flow plates found in larger fuel cells, while others have focused on reducing or eliminating the separator membrane. In the former class, Smyrl has published several papers based upon using a thin Si membrane that has micromachined holes through the thickness of the membrane to act as a catalyst support and gas diffusion layer. Electrocatalysts are subsequently either deposited onto these microporous membranes

* Corresponding author. Tel.: +1 505 844 3497; fax: +1 505 284 6720.
 E-mail addresses: caapble@sandia.gov (C. Apblett), dingers@sandia.gov
(D. Ingersoll), plamen@unm.edu (P. Atanassov), donmaricle@att.net
(D. Maricle), S-sarangapani@verizon.net (S. Sarangapani).

[1], or painted onto the separator directly as has been traditionally in large-scale fuel cells [2,3]. In either case, these Si end plates are then and then sandwiched on either side of a Nafion 117 membrane. Good performance, approaching that of larger scale fuel cells, is demonstrated, but at very vigorous conditions (0.25 cm^2 of active area with 200 ml min^{-1} flow rate of MeOH), which indicates a relatively low fuel utilization efficiency within the cell. It is likely that these conditions are necessary in order to overcome the diffusion limitations through the microchannels, where stagnant, diffusion limited transport of methanol from the reservoir to the catalytic surface must occur through these small micropatterned channels, and thus high fuel supply rates are required to overcome this transport. Nevertheless, a methanol/forced air power level of roughly 40 mW cm^{-2} is demonstrated at 0.35 V, and upwards of 60 mW cm^{-2} is demonstrated at maximum power, which is close to the values reported for large cells of 75–80 mW cm^{-2} realized by the Los Alamos team [4]. Kohl et al. [5] have also used a high surface area catalyst in his work with microchannels, but has separated the catalytic layer from the ionic conductive layer for fabrication purposes. He has then replaced the lost ionic contact between catalyst and ionomer by acidifying the incoming fuel stream. While this allowed for excellent miniaturization of the system (allowing for an 18 μm wide catalytic area), performance from this type of cell was significantly below that reported for large scale cells, and showed only a 0.35 V open circuit response (OCV) with a maximum power delivered of 15 μW cm^{-2} at 80 °C.

Other workers [6] have opted to use direct evaporated catalysts in an effort to make the process monolithically integrated fuel cells, but have shown drastically reduced performance as a result (0.78 mW cm^{-2}). The fuel supply rate on this system were quite low, only 10 μl min^{-1}, but the active area over which the flow was passed was also low, at 0.018 cm^2 of active area. Scaled to consider the flow as a supply per square centimeter of active area, the supply of fuel here is roughly 500 μl min cm^{-2} of active area.

Still other attempts to miniaturize fuel cells capitalized on the concept that flow through channels at the microdimension is almost always laminar [7] to remove the ionic separator within a fuel cell and replace it with a flowing separator of acid or alkaline media to replace the ionic conduction path. Kenis [8] and Whitesides [9] have used this laminar flow separation between the anode and cathode to good effect in microchannels, where a moving channel of acid resulted in a much higher ion exchange capacity when compared to an ionomer. However, power from these cells was not as high as would be expected from the loss of the crossover losses and the increased ion exchange capacity, with power levels in the 20–30 mW cm^{-2} range.

Since the majority of the volume of a fuel cell is not contained within the electrode structures or the separator membrane, targeting these structures for miniaturization will not yield a significant loss in volume of the cell. If, however, the membrane, electrode, and gas diffusion layers of the fuel cell remain identical in structure and thickness to large-scale fuel cells, performance within these layers commensurate to larger scale fuel cells can still be reasonably expected. What remains, then, is to miniaturize the largest volume portion of the fuel cell, which would be

the flow fields, seals, and current collectors. These components are typically made of graphite or stainless steel in large cells, with graphite being preferred due to the electrochemical inertness of the material under harsh fuel cell operating conditions. We have focused on developing robust, reliable miniature fuel cell end plate hardware from graphite that is compatible with traditional membrane electrode assembly (MEA) architectures. In this work, we report on the design and fabrication of the miniature fuel cell hardware that is designed for hydrogen/oxygen performance, as well as some data on the performance of these miniature cells using methanol and oxygen.

2. Design and experimental

Most large-scale fuel cells use either coated stainless steel or graphite for the end plate material. These materials are selected due to their good electrical conductivity and relative electrochemical inertness. These plates are relatively thick, however, and comprise up to 95% of the volume of larger fuel cells. For large-scale fuel cells, this large thickness ensures that even compression pressure can be applied on the seals and active area of the fuel cell with little mechanical deformation of the end plates. In a miniature cell, however, mechanical deformation can no longer be ignored. Stainless steels, though more compliant than graphite, has been shown to suffer from corrosion issues under long operational times, and requires an inert coating (such as Au) in order to avoid this. This can cause problems in the conductivity of the cell, which would be exacerbated in the small fuel cell size. For these reasons, graphite end plates were chosen for this application.

For all of the experimental methods described below, only a single fuel cell was being assembled, although the technique could be applied to the building of a cell stack, as well. Thinned plates (0.5 mm thick) of nonporous, high purity graphite were obtained from POCO, Inc. Three designs were fabricated into the plates. The first was an internally manifolded, straight channel plate with 250 μm wide channels separated by 250 μm wide ribs. These ribs were recessed into the plate by 100 μm, to allow space for a traditional 175 μm thick gas diffusion layer. In the second design, the channel and rib widths were widened to 1 mm each, and the center recess to accommodate the gas diffusion layer was removed, with the GDL accommodated by gaskets. In the final design, a single channel serpentine design with 1 mm wide channel on 0.5 mm wide ribs was fabricated and matched to the same basic header as was used in the previous two designs. An optical image of each of these designs is shown in Fig. 1.

Machining of the flow field into these plates was accomplished by ultrasonic milling at an offsite facility (Bullen Ultrasonics, OH). To fabricate these plates, a negative master mold of the pattern to be machined into the plates is made through plunge wire electric discharge milling (EDM). This negative master is then mounted to an ultrasonic horn; a slurry of 0.3 μm alumina slurry is passed over the graphite plate, and the negative master is pressed, under ultrasonic vibration, against the graphite. The vibration causes the alumina slurry to grind away the graphite, resulting in a positive pattern being etched into the graphite plate by the ultrasonic grinding action. This process
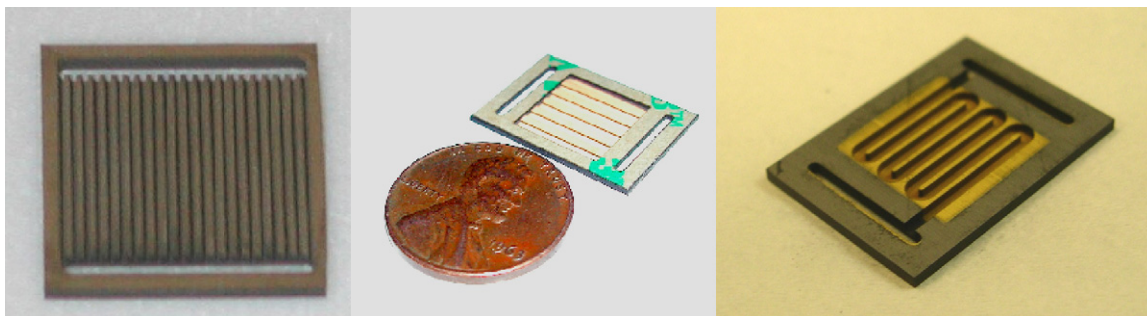
Fig. 1. Separate designs of flow plates through the generations: 250 mm channels with 250 μm ribs (far left), 1 mm channels with 1 mm ribs (center), 1 mm channnel with 500 μm ribs in a single serpentine (right). Each end plate is roughly the same size, with the same active area (1 cm^2). The center plate has an acetate gasket in place on the plate.

was relatively inexpensive, and could be used to mass produce large numbers of plates from a single master. The smallest resolution achievable with this technique, however, was 250 μm, as the ultrasonic vibration amplitude resulted in a 50 μm tolerance for the parts.

Since standard cell membrane and electrode assemblies (MEAs) are already quite thin (roughly 0.5 mm thickness per MEA), it was decided to use standard configuration and thickness MEA structures within the cell, to minimize power losses due to structural changes within the gas diffusion layer, electrode layer, and membrane interfaces. This also allowed a direct comparison between the performance of larger scale fuel cells and the miniaturized cell, since identical MEA structures were in use. For this technique, fabrication of the electrode structure employed a mixture of platinum (for the cathode structure) or platinum–ruthenium (for the anode structure), Nafion® dissolved in a solution of alcohols, and a Teflon® binding agent. These three components were mixed together and mechanically treated to drive off the solvent structure, leaving behind a porous, claylike material. This material was then pressed to the final use thickness (in this case, 50 μm), and pressed against the gas diffusion layer. The gas diffusion layer was commercially available Toray™ paper. Once the catalyst layer was pressed to the diffusion layer, the combined electrode/gas diffusion layer structure was cut to a 1 cm × 1 cm area for the active electrodes.

A piece of 175 μm thick fully hydrated Nafion® was used as the proton exchange membrane (PEM). The previously fabricated electrode/gas diffusion layers (GDL) were placed on either side of the hydrated membrane, and this assembly stack, consisting of the Toray® paper for the anode, the Pt–Ru electrode, the Nafion® separator, the Pt cathode electrode, and the cathode Toray® paper, was then placed into a hot press, and compressed at 130 °C to diffuse the electrode structures into the Nafion, and decrease the interfacial impedance at this interface. For all the electrodes used in this work, the cathode was never varied from being a pure Pt black electrode structure and the anode catalysts was Pt–Ru black. A loading of 6 mg cm^{-2} of Pt black was used in the cathode, while the anode was loaded with 5 mg cm^{-2} of Pt–Ru black.

Seals were prepared from a thin commercially available adhesive (50 μm thick VHB™ adhesive tape from 3 M), laser cut into a pattern that allowed for seals to be created around the edge of

the plates and the manifolds, while leaving the channels and the connections to the manifold uncovered. A total thickness of 50 μm (for earlier designs) to 150 μm (for later designs) of tape was used to create the seals on both the anode and cathode side by first applying the seal to the end plate. The MEA assembly was placed against the seal ring, and lightly compressed to allow the adhesion of the tape to hold the MEA in place. The anode end plate was then assembled with an adhesive ring seal and pressed against the anode gas diffusion layer and lightly compressed to seat the seal ring against the membrane. Once complete, this assembly is then compressed in a conventional press. The daylight gap is reduced until a force is detected on the load cell of the chucks, which indicated that the cell was now clamped by the chucks. An additional ~75 μm of displacement was then placed on the chucks to compress the cell. This displacement typically results in a load force of around 600 psi on the end plates. Most of the displacement is taken up in the difference between the height of the gaskets from the membrane (150 μm nominal) and the height of the Toray™ gas diffusion layer (GDL) and electrode (225 μm nominal). When the cells were disassembled after testing, a permanent footprint of roughly 50 μm was present in the backs of the GDL, indicating reasonable compression and interface between the flow field and the GDL. In Fig. 1, the center plate is shown with a gasket already in place on the end plate.

Assembled cells were preconditioned prior to testing by holding the cells at 80 °C for 24 h with 20 sccm of fully humidified hydrogen and 20 sccm of oxygen, with a fixed potential of 0.5 V across the cell. This potential would typically result in a current of roughly 400–500 mA cm^{-2} across the cell.

3. Results and discussion

To characterize the performance of the cell assemblies, the cells were first tested in hydrogen and oxygen. Each of the three flow plates was built into a full cell with identical active areas and using identical MEA assemblies. The polarization curves for each of the cells are shown in Fig. 2. When voltage is plotted against the normal log of the current, the low current region (between 1 and 100 mA) is demonstrative of the oxygen kinetics, and is normally reported at a value of 72 mV dec^{-1} [10]. As seen in Fig. 2, where the polarization curves are plotted in this
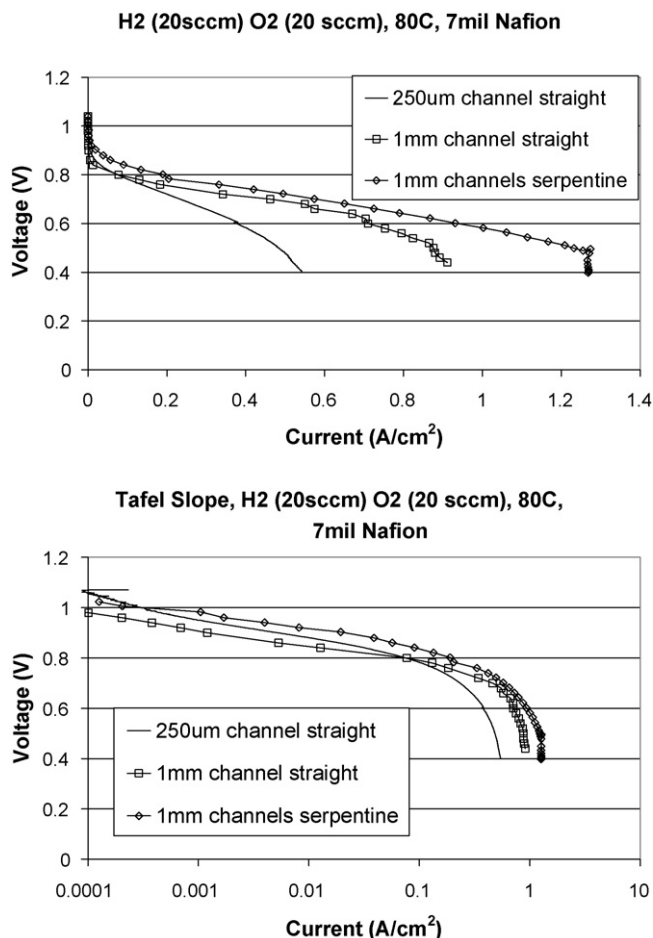
H2 (20sccm) O2 (20 sccm), 80C, 7mil Nafion

Tafel Slope, H2 (20sccm) O2 (20 sccm), 80C, 7mil Nafion

Fig. 2. Performance of cells built with each end plate, using standard MEAs built using 7 mil Nafion. Conditions—anode: 5 mg cm^{-2} Pt–Ru, 20 sccm H$_2$, cathode: 6 mg cm^{-2} Pt, 20 sccm O$_2$, 80 °C. (a) Tafel slope of cells built with each end plate, showing polarization of 70 mV decade^{-1} for each cell. Conditions—anode: 5 mg cm^{-2} Pt–Ru, 20 sccm H$_2$, cathode: 6 mg cm^{-2} Pt, 20 sccm O$_2$, 80 °C.

fashion, all of the plates exhibit a Tafel region slope of this value, indicating good kinetics on the electrode, and appropriate supply of oxygen, since there is no early "break" in the curve, indicating early onset of mass transport limitations on the cathode.

In the case of the 250 μm wide channel end plate, however, the onset of discernable mass transport limitation does begin shortly after 100 mA cm^{-2} is reached, which is well before this effect was observed in the larger channel width cells. Most of the mass transport polarization of the hydrogen oxygen cell can be attributed to the transport of oxygen to the catalyst at high current densities under normal conditions [11]. If oxygen transport limitations are limiting the high current regions of the polarization curve in Fig. 2, then this may be explained as the onset of water formation on the cathode causing partial blockages of the cell flow field, which limits further oxygen supply to the catalytic layer [12]. This would explain the dependence on the size and shape of the flow field as well, since the smaller channels would be more susceptible to blocking by the precipitation of water droplets within the cathode channels, leading to an early onset of mass transport limitations.
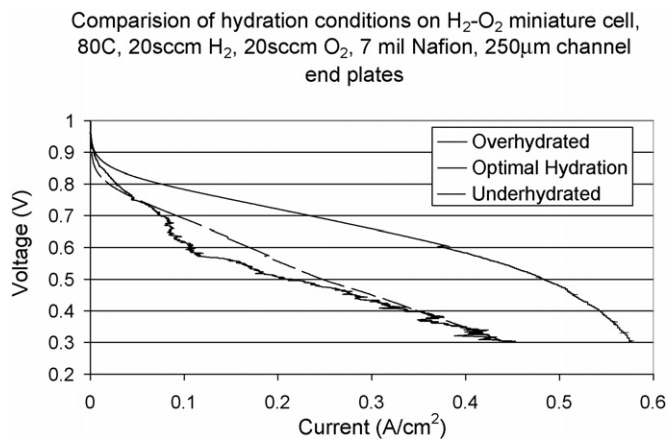
Comparision of hydration conditions on H$_2$-O$_2$ miniature cell, 80C, 20sccm H$_2$, 20sccm O$_2$, 7 mil Nafion, 250μm channel end plates

Fig. 3. Cell performance with smallest channels, showing effect of 20% over and 20% underhydration on power delivered. Conditions—anode: 5 mg cm^{-2} Pt–Ru, 20 sccm H$_2$, cathode: 6 mg cm^{-2} Pt, 20 sccm O$_2$, 80 °C.

Since the flow rates for these cells are relatively low, the pressure drop through the channels is very small (no difference in pressure between an inlet and outlet pressure monitor), there is little force available to unblock the parallel flow channel cells. It should be noted, however, that although the flow rates are small, the flow stoichiometry conditions, calculated in the manner of Kunz et al. [13] is quite high, at a value of 5.2 at a current of 1 A cm^{-2}. Therefore, it is unlikely that the actual flow of oxygen is limiting the current of the cells, but instead the diffusion of oxygen to the catalyst surfaces is likely inhibited by water droplets that form within the channels. Since there is a low flow rate and little pressure drop to drive the water out of the parallel channel cell, any blockage in the parallel channel system will result in an early onset of mass limitation.

This is in contrast to the serpentine channel flow field, where any blockage in the flow field will result in a flow stoppage until sufficient pressure in built up that the water droplet can be forced from the cathode flow field. Since this design is not susceptible to water blockage, much higher currents are supported. The ultimate current limitation at 1.3 A cm^{-2} is at an oxygen stoichiometry of four, which is still above limiting stoichiometry reported in the literature [14]. This indicates that other mass transport limiting factors, such as water condensation within the microporous layer of the electrode itself at high currents, may be limiting the rate capacity of the cathode [15].

One way of testing whether or not water blockage is having a significant effect on mass transport within the flow fields is to look at the effect of hydration on the cell performance. In this case, the 250 μm flow channels plates were used, which are expected to exhibit the most pronounced effect of water condensation in the small channels. Three stable operating conditions were set up on a cell running hydrogen-oxygen at our standard conditions, but in this case, the oxygen flow was purposefully either overhydrated or underhydrated by using a dewpoint water saturation system, as has been described elsewhere. [16] The results of these tests for a fuel cell held at 80 °C are shown in Fig. 3. The curve for optimal hydration is the same curve as was reported in Fig. 2 above, with hydration conditions optimized

to produce the maximum power, which was 63% RH on the cathode. The other two data sets in Fig. 3 represent polarization curves taken at 20% over and 20% under this optimal humidity value for the cathode. For the underhydrated condition, the curve is smooth, but the ohmic region of the curve has a higher slope than that of the optimally hydrated region. This indicates that, as expected, the membrane is operating under reduced humidity conditions, with a resultant increase in the membrane resistance, since the hydronium concentration is necessarily lower in the less humidified membranes [17,18].

For the overhydrated condition, the curve is somewhat erratic and jagged. The slope for this curve is again higher, though it is unlikely that this is due to a higher resistivity, as in the case of the underhydrated condition. In this case, overhydration of the cathode can result in the generation of excess water during high current operation. In the small channels that were used for this test, the precipitation of water droplets would be likely to block the flow channels of the fuel cells, resulting in a decrease in the supply of oxygen to the cathode [19,20]. The lowering of the oxygen supply results in a decrease in the current of the cell, as mass transport limitation on the cathode results in an early onset of the limiting current, which lowers the current of the overall device. As a result of this, less water is generated at the cathode under lower current, and the water blockage may be removed as the water is removed. Once the blockage is removed, the mass transport limitation of the oxygen is removed, and the current once again increases to the previous level, and the water generation at the cathode increases as well. This oscillation between water formation and water blockage removal can result in the jagged appearance of the polarization curve seen in Fig. 3 for the overhydrated state. Since the cell is operating at all times in a situation of early mass transport limitation on the cathode, the polarization curve will show a lower current at a given voltage. This reduced current has the effect of appearing on a polarization curve as an increase in the slope of the ohmic region of the curve.

Operation of the miniature fuel cell was also tested using a one molar methanol fuel mixture using the three different end plate configurations. The results of these tests are shown in Fig. 4. As was seen in the case of the hydrogen oxygen fuel cells, the methanol oxygen fuel cells followed the same trend of lower performance for narrow channels as opposed to wider channels, and better performance from serpentine flow channels than from parallel straight channels. The performance of the linear flow fields was significantly below the performance of large scale cells operating under these conditions, but the serpentine design demonstrated performance of $140 \, \mathrm{mW \, cm^{-2}}$. This value is approximately 70% of the value reported for methanol fuel cells operating with oxygen at 60 psi. and higher temperature [21]. The difference between the performance of this fuel cell and large-scale fuel cells may be due to the fact that the small-scale fuel cells were operated at room pressure oxygen rather than at elevated pressure, and the temperature difference between the two tests. The performance of this cell is above that reported by Liu et al. [22] for similar conditions and flow rates ($80 \, \mathrm{mW \, cm^{-2}}$ at $0.1 \, \mathrm{ml \, min^{-1}}$ MeOH, 1 M, 60 °C, oxygen cathode), but the trends noted in Liu's work, namely the effect
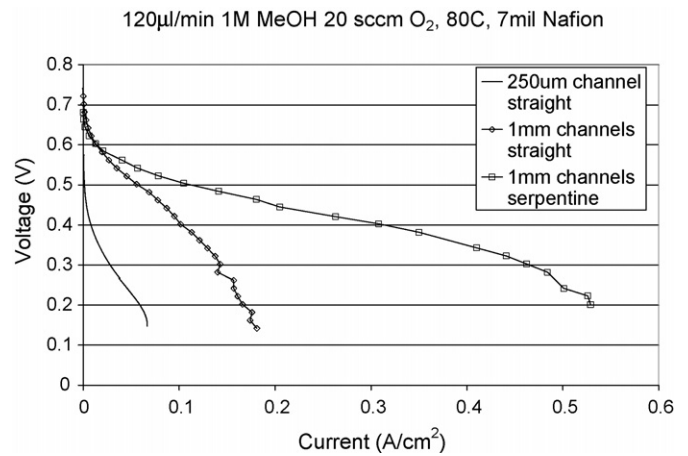
Fig. 4. Cell performance of three different plates using 1 M methanol. Conditions—anode: $5 \, \mathrm{mg \, cm^{-2}}$ Pt–Ru, $0.12 \, \mathrm{ml \, min^{-1}}$ 1 M MeOH, cathode: $6 \, \mathrm{mg \, cm^{-2}}$ Pt, 20 sccm O$_2$, 80 °C.

of the width and shape of the flow fields, is in agreement with that which is reported here.

The lower operation of the linear channel fuel cells may be interpreted similarly to the performance trends noted in the case of the hydrogen performance.

Fuel utilization for MeOH operation can be calculated from the known flow rate through the system and the number of electrons involved in the reaction. For all the data reported here, the flow rate was a constant $0.12 \, \mathrm{ml \, min^{-1}}$ flow rate. Calculating the theoretical current capacity from a modification of the equations used by Liu and Zhao [23] gives

$$i_{\mathrm{th}} = nQCF \qquad (1)$$

where i_{th} is the theoretical current density, n the number of oxidized electrons, Q the flow rate of the fuel through the system, C the concentration of the fuel, and F is the Faraday's constant. The fuel utilization of the system, then, would just be the actual measured current density at a given voltage divided by the theoretical current density at that fuel supply rate. For the systems measured in Fig. 4, the fuel utilization efficiency is calculated to be only 1.4% for the 250 μm straight channels, 10.8% for the 1 mm straight channels, and 34.5% for the 1 mm serpentine channels. While this is low compared to some larger systems [24], it compares well with fuel utilization reported for most DMFC systems that are single pass [25,26].

Most of the literature reported for direct methanol fuel cells does not use oxygen, but rather reports on using air based cathodes (either supplied at pressure or passively from the atmosphere). The performance of this cell operating on atmospheric pressure air, as opposed to oxygen, is shown in Fig. 5. The performance of this cell is roughly $75 \, \mathrm{mW \, cm^{-2}}$ under these conditions, which is in good agreement with the performance associated with large direct methanol fuel cells at similar conditions [27]. It is interesting to note that the polarization associated with the use of air versus oxygen in these measurements is approximately 80 mV at $200 \, \mathrm{mA \, cm^{-2}}$, but increases after this current value. This polarization is slightly higher than what has been reported in the literature previously (for hydrogen
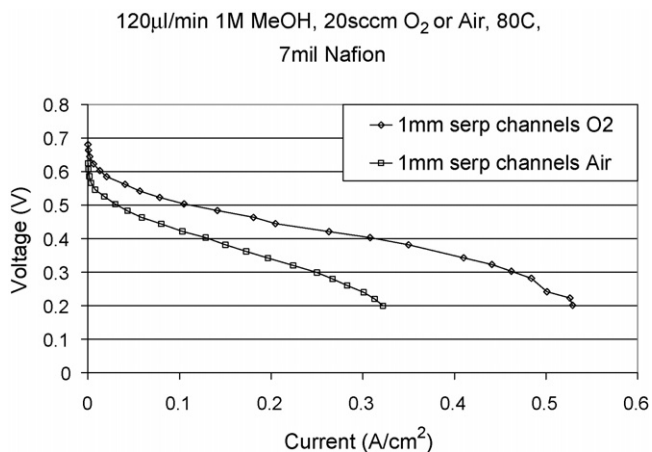
120μl/min 1M MeOH, 20sccm O₂ or Air, 80C, 7mil Nafion

Fig. 5. Cell performance of 1 M methanol serpentine plates using oxygen and air. Conditions—anode: 5 mg cm^{-2} Pt–Ru, 0.12 ml min^{-1} 1 M MeOH, cathode: 6 mg cm^{-2} Pt, 20 sccm O₂ or air, 80 °C.

Time dependence of HFR, 20sccm O₂, 7mil Nafion, 2mil acetate seal

Fig. 7. High frequency resistance (HFR) measurements of hydrogen and methanol cells over time, showing aging dependence of HFR. Conditions—anode: 5 mg cm^{-2} Pt–Ru, 20 sccm H₂ or 0.12 ml min^{-1} 1 M MeOH, cathode: 6 mg cm^{-2} Pt, 20 sccm O₂ or air, 80 °C.

fueled cells) [28], which may be associated with the higher than expected resistances within the cell and the increased internal polarization due to internal resistances.

To investigate the possibility of a small internal resistance causing the slightly higher polarizations associated with these small fuel cells, high frequency resistance (HFR) measurements were taken on the cells under various operating conditions, and the data are shown in Fig. 6. The method to obtain these data is a current interrupt method, and has been reported in the literature previously [29]. Reported values for the internal resistance for hydrogen fuel cells are roughly 0.2 Ω cm^{-2} at high voltages, increasing to 0.4 Ω cm^{-2} at lower voltages [30]. For the miniature cells reported here, serpentine channels start out in good agreement with the literature (∼0.25 Ω cm^{-2} at OCV), but climb above 0.45 Ω cm^{-2} at currents in excess of 1 A cm^{-2}. The increase in HFR is usually associated with dehydration at the anode under increased current loads, as electrosmotic drag dries the anode out, increasing the series resistance of the mem-

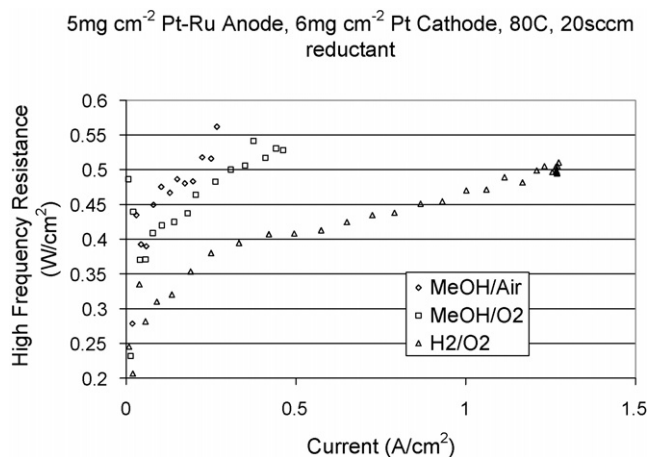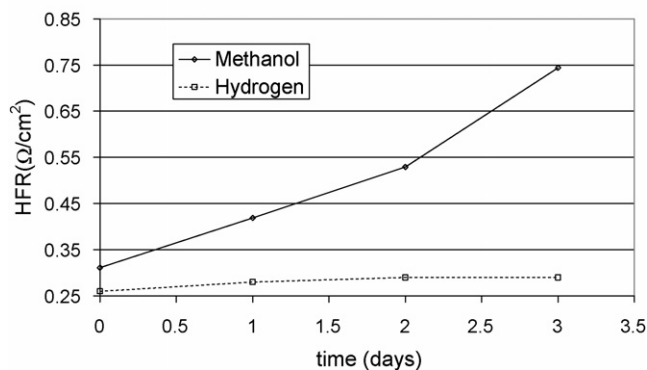5mg cm⁻² Pt-Ru Anode, 6mg cm⁻² Pt Cathode, 80C, 20sccm reductant

Fig. 6. High frequency resistance (HFR) measurements of hydrogen and methanol cells under various conditions, showing current dependence of HFR. Conditions—anode: 5 mg cm^{-2} Pt–Ru, 20 sccm H₂ or 0.12 ml min^{-1} 1 M MeOH, cathode: 6 mg cm^{-2} Pt, 20 sccm O₂ or air, 80 °C.

brane at higher currents. This effect should be compensated for by using methanol as the fuel, since water is continually replenished at the anode from the fuel supply. The data in Fig. 6 for both the air and oxygen case of methanol do not agree with this, however. In the case of the methanol fuel cell, normal open circuit HFR is typically below 100 mΩ, but for the cell reported here, the value is closer to 400 mΩ, with a much more rapid increase under higher current loads. Since the membrane hydration is unlikely, in this case, to be the cause of this, the resistance increase from hydrogen to methanol must be due to some other factor increasing the internal series resistance.

High internal cell resistance can come from an increase in the interfacial impedance between the end plate and the gas diffusion layer, or between the electrode layer and the gas diffusion layer, or between the electrode catalyst layer and the membrane. Since the gas diffusion layer and electrode catalyst layer are prepared in the same manner in both the hydrogen and methanol case, it is unlikely that variations here can be causing the changes in the measured HFR. An increase in the interfacial resistance is possible, however, due to the nature of the sealing material between the membrane and the flow field end plate.

As mentioned in the experimental section, the fuel cell is held together using a acetate seal that provides both the liquid and gas seal on the anode and cathode, and also serves to provide the mechanical structure to hold the cell together. While operating in a hydrogen environment, dimensional change of the acetate seal is small, since uptake of water in the acetate is minimal. However, the acetate can absorb methanol easily, and leads to large dimensional changes in the acetate [31,32]. By absorbing methanol, the acetate seals will expand and separate the current collector end plate away from the gas diffusion layer, thereby increasing the interfacial resistance and causing a drop in the performance of the cell over time. This is shown in the data in Fig. 7, where the HFR for the methanol and hydrogen fuel cell under nominal current (∼200 mA cm^{-2}) is shown as a function of days of operation. For the hydrogen case, no swelling is expected in the seals, and the change in the HFR

is on the order of only ~10%, which is likely to be related to stress relaxation on the polymer acetate seal. However, in the methanol case, the change is on the order of ~150%. It is possible, given the response of the acetate to methanol in the fuel stock, that this is the source of the increased HFR noted in the methanol performance of the cell, versus the performance in the hydrogen.

4. Conclusions

We have built and tested a miniaturized hydrogen/oxygen fuel cell that has achieved power densities close to those reported for large fuel cells operating under enhanced conditions, and requiring no external compression for operation. The seal gaskets are made of a thermoplastic adhesive that is laser cut to seal both the internal manifolds as well as the external surface. The gaskets are only 50 μm thick, and provide compression for the end plates to the gas diffusion layer as well as the membrane. Individual cells assembled using this technique produce a maximum power of approximately 600 mW at 80 °C from 20 sccm of fully hydrated hydrogen and oxygen. Water management in the small channels is shown to be power limiting, as water condensation on the cathode leads to a very early onset of mass transport limitation for the oxygen. The onset current for mass transport limitation can be increased by widening the channels, with more narrow channels suffering more acutely from water management, possibly due to the increased capillary forces present in these smaller channels. Methanol performance in single miniaturized cells has been shown to produce over 140 mW of power from 1 M methanol using 120 μl min^{-1} at 80 °C with oxygen reductant, and 75 mW under similar conditions using air. Fuel utilization for the cells was able to achieve as high as 34% using a single pass configuration.

Data from the methanol experiments indicated that hydration alone cannot explain the higher resistances of the smaller cells, and that compression and interfacial resistances need to be improved for use in small scale fuel cells. It is unclear at this point what the source of the increased HF resistances are in small scale cells, but at least some evidence points to a higher interfacial impedance of the membrane interfaces and the need to be have better compression in small scale cells than is necessary in an equivalent palmscale fuel cell.

Acknowledgement

References

[1] S.C. Kelley, G.A. Deluga, W.H. Smyrl, J. AlChE 48 (5) (2002) 1071–1082.
[2] S.C. Kelley, G.A. Deluga, W.H. Smyrl, Electrochem. Solid-State Lett. 3 (9) (2000) 407–409.
[3] M.S. Wilson, S. Gottesfeld, J. Appl. Electrochem. 22 (1992) 1–7.
[4] X. Ren, P. Zelenay, S. Thomas, J. Davey, S. Gottesfeld, J. Power Sources 86 (2000) 111–116.
[5] J. Li, C. Moore, P. Kohl, J. Power Sources 138 (2004) 211–215.
[6] S. Motokawa, M. Mohamedi, T. Momma, S. Shoji, T. Osaka, Electrochemistry 73 (5) (2005) 346–351.
[7] R.F. Ismagilov, A.D. Stroock, P.J.A. Kenis, G. Whitesides, H.A. Stone, Appl. Phys. Lett. 76 (17) (2000) 2376–2378.
[8] E.R. Choban, J.S. Spendelow, L. Gancs, A. Wieckowski, P.J.A. Kenis, Electrochim. Acta 50 (2005) 5390–5398.
[9] R. Ferrigno, A.D. Stroock, T.D. Clark, M. Mayer, G.M. Whitesides, J. Am. Chem. Soc. 124 (2002) 12930–12931.
[10] M.V. Williams, H.R. Kunz, J.M. Fenton, J. Electrochem. Soc. 152 (3) (2005) A635–A644.
[11] M.L. Perry, J. Newman, E.J. Cairns, J. Electrochem. Soc. 145 (1) (1998) 5–15.
[12] P. Berg, K. Promislow, J. St. Pierre, J. Stumper, B. Wetton, J. Electrochem. Soc. 151 (3) (2004) A341–A353.
[13] M.V. Williams, H.R. Kunz, J.M. Fenton, J. Power Sources 135 (2004) 122–134.
[14] H.A. Gasteiger, J.E. Panels, S.G. Yan, J. Power Sources 127 (2004) 162–171.
[15] A. Kazim, P. Forges, H.T. Liu, Intl. J. Energy Res. 27 (2003) 401–414.
[16] D. Hyun, J. Kim, J. Power Sources 126 (2004) 98–103.
[17] P. Berg, K. Promislow, J. St. Pierre, J. Stumper, B. Wetton, J. Electrochem. Soc. 151 (3) (2004) A341–A353.
[18] T. Thampan, S. Malhotra, H. Tang, R. Datta, J. Electrochem. Soc. 147 (9) (2000) 3242–3250.
[19] J.J. Baschuk, L. Xianguo, J. Power Sources 86 (1) (2000) 181–196.
[20] X.G. Yang, F.Y. Zhang, A.L. Lubawy, C.Y. Wang, Electrochem. Solid-State Lett. 7 (11) (2004) A408–A411.
[21] M. Baldauf, W. Preidel, J. Power Sources 84 (1999) 161–166.
[22] C.W. Wong, T.S. Zhao, Q. Ye, J.G. Liu, J. Electrochem. Soc. 152 (8) (2005) A1600–A1605.
[23] J.C. Liu, T.S. Zhao, Z.X. Liang, R. Chen, J. Power Sources 153 (1) (2006) 61–67.
[24] A.S. Arico, P. Creti, V. Baglio, E. Modica, V. Antonucci, J. Power Sources 91 (2000) 202–209.
[25] E.R. Choban, J.S. Spendelow, L. Gancs, A. Wieckowski, P.J.A. Kenis, Electrochim. Acta 50 (2005) 5390–5398.
[26] S.C. Kelley, G.A. Deluga, W.H. Smyrl, AIChE J. 48 (5) (2002) 1071–1082.
[27] X. Ren, P. Zelenay, S. Thomas, J. Davey, S. Gottesfeld, J. Power Sources 86 (2000) 111–116.
[28] M. Williams, H.R. Kunz, J.M. Fenton, J. Electrochem. Soc. 152 (3) (2005) A635–A644.
[29] M. Smith, K. Cooper, D. Johnson, L. Scribner, Fuel Cell 5 (2) (2005) 26–31.
[30] Q. Dong, J. Kull, M.M. Mench, J. Power Sources 139 (2005) 106–114.
[31] M. Sanopoulou, J.H. Petropoulos, Polymer 38 (23) (1997) 5761–5768.
[32] G. Gozzelino, G. Malucelli, Coll. Surf. A., Physico. Eng. Aspt. 235 (2004) 35–44.